# Crust and upper mantle velocity structure of the Yellowstone hot spot and surroundings

Derek L. Schutt,[1] Ken Dueker,[1] and Huaiyu Yuan[1]

Received 11 April 2007; revised 21 September 2007; accepted 30 November 2007; published 28 March 2008.

[1] The Yellowstone hot spot has recently been shown to be a plume that extends into the transition zone. At roughly 60–120 km depth, the plume material rising beneath Yellowstone Park is sheared SW by North America Plate motion, producing a profound low velocity layer emplaced beneath the thin lithosphere. To constrain the absolute seismic velocity of the plate-sheared plume layer, fundamental mode Rayleigh wave observations have been inverted for phase velocity using the two plane wave technique. The resulting phase velocity models are inverted with Moho-converted *P* to *S* arrival times to better constrain crustal thickness and absolute *S* wave velocity structure to ~120 km depth. A regionalized *S* wave velocity model has an extremely low velocity minimum of 3.8 ± 0.1 km/s at 80 km depth beneath the hot spot track. Nonregionalized 3-D velocity models find a velocity minimum of 3.9 km/s beneath the hot spot track. Below 120 km depth, our resolution diminishes such that the lateral spreading of the plume track is not resolved. The volume of the low velocity plume layer is small and the estimated buoyancy flux for the Yellowstone plume is <0.1 Mg/s which contrasts with the ~9 Mg/s value for Hawaii. In addition, a notable region of thick crust and high lower crustal velocities is found around Billings, Montana, consistent with previous refraction and receiver function studies that interpret this as evidence for a massive Precambrian underplating event.

**Citation:** Schutt, D. L., K. Dueker, and H. Yuan (2008), Crust and upper mantle velocity structure of the Yellowstone hot spot and surroundings, *J. Geophys. Res.*, *113*, B03310, doi:10.1029/2007JB005109.

## 1. Introduction

[2] Over the last ~17 Ma, the Yellowstone hot spot has produced a series of progressively younger silicic eruptions that extend from the Oregon-Nevada border NE to Yellowstone National Park [*Christiansen and Yeats*, 1992]. Because the Yellowstone hot spot track (YHT; Figure 1) lies in a region of extensive recent magmatism, including the Columbia River Basalts and the Oregon High Lava Plains, the cause of the hot spot magmatism has remained controversial. This anomalous magmatism has been variously hypothesized to be an extending lithospheric crack [*Hamilton*, 1989; *Christiansen et al.*, 2002], a self-propagating mantle melt instability [*Humphreys and Dueker*, 1994], or a thermal mantle plume [*Armstrong and Leeman*, 1975; *Morgan et al.*, 1984]. Recently, *P* and *S* wave tomography studies [*Yuan and Dueker*, 2005; *Waite et al.*, 2006] have found a low velocity conduit extending from Yellowstone Park and inclined 15° from vertical toward the NW. The base of the conduit extends into a locally thinned transition zone [*Fee and Dueker*, 2004] but does not extend across the 660 km discontinuity. This structure is consistent with a thermal plume confined to the upper mantle. At ~60–120 km depth beneath the YHT, this plume material has been sheared to the SW by North America plate motion, producing a profoundly low velocity region beneath the YHT associated with some combination of high temperatures and partial melt [*Schutt and Humphreys*, 2004]. Although ascending plume material interacting with a moving lithosphere is predicted to follow parabolic-like streamlines [*Sleep*, 1990], the observed Yellowstone velocity anomaly does not follow parabolic-like streamlines downstream from the present location of the hot spot under Yellowstone Park [*Saltzer and Humphreys*, 1997; *Schutt and Humphreys*, 2004; *Yuan and Dueker*, 2005; *Waite et al.*, 2006]. In addition, a parabolic-like distribution of fast SKS wave polarization axes is not observed [*Waite et al.*, 2005]. The above observations all suggest the YHT is the manifestation of a weak upper mantle plume with little buoyancy induced lateral flow at the base of the lithosphere.

[3] The previous teleseismic body wave tomographic models all have limitations, however. Only relative velocity variations are constrained, which makes it difficult to compare absolute velocities to other regions or calculate absolute temperature. In addition, the previous body wave tomograms do not resolve crustal velocity and thickness variations, and the tomograms' best-case ~40 km vertical resolution scale is poor with respect to surface wave studies [e.g. *West et al.*, 2004]. In this study, we measure the velocity of fundamental mode Rayleigh waves in the region. These data are combined with measurements of the relative arrival time difference between receiver function direct *P*

[1]Department of Geology and Geophysics, University of Wyoming, Laramie, Wyoming, USA.


0148-0227/08/2007JB005109$09.00

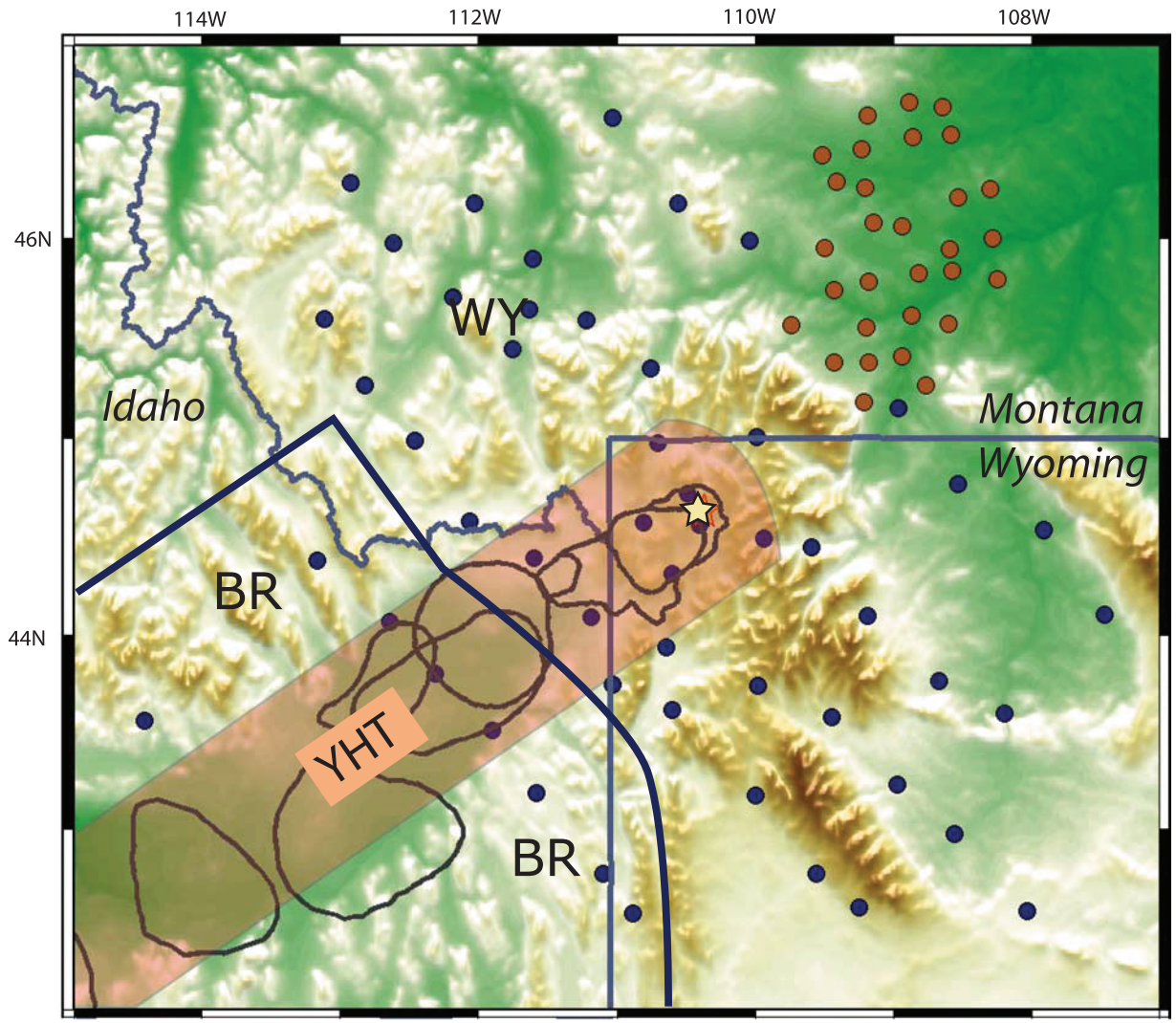


**Figure 1.** Topography, seismic stations, and velocity model regionalization. Seismic sites are denoted as colored dots: Yellowstone array (blue), Billings array (red). The partitioning of the region into three domains is shown by the pink shaded area (YHT), the thick blue line (BR), and the rest of the region (WC). The last 12 Ma of volcanic calderas along the hot spot track are outlined, and the Sour Creek dome, roughly the current location of the hot spot, is marked with a star.

and $P_m$s arrivals to produce models of absolute *S* wave velocity and crustal thickness variations.

## 2. Data

[4] Data were derived from two broadband PASSCAL experiments that operated in late 1999–2001 and whose recording times overlapped by 75 d (Figure 1): the 46 station Yellowstone array and the 31 station Billings array (Figure 1). These arrays operated from 9 June 2000 to 4 June 2001 and 30 September 1999 to 23 August 2000, respectively. The arrays were instrumented with CMG-3T, CMG-40T, and STS-2 sensors with corner periods at 120, 30, and 120 s. Careful attention was paid to transfer function normalization and channel polarity because the two-plane-wave technique [*Forsyth and Li*, 2005] fits both the Rayleigh wave's amplitudes and phase with equal weight.

[5] Events with surface-wave magnitudes >5.7, from distances of $30^\circ \leq \Delta \leq 120^\circ$, were examined for simple fundamental mode Rayleigh wave packets at 17 wave periods between 15 and 150 s. To measure phase velocities at the 17 periods used in this study, seismograms were narrowband (10 mHz width) filtered with a zero-phase four-pole Butterworth filter. The filter center periods were at 15, 18, 20, 22.5, 25, 27.5, 30, 35, 40, 45, 50, 66, 75, 90, 110, 125, and 150 s. Band-pass filtered traces without a relatively simple fundamental mode Rayleigh wave envelope were rejected. This data culling produced 81 events to be analyzed, although for any given event, measurable Rayleigh wave energy was not generally observed at all periods. For most periods, 50–60 events were analyzed (Table 1) which provided data from a reasonable range of back-azimuths (Figure 2). Traces were converted to their Fourier real and imaginary components at each filter center period. Therefore, each station-event seismogram provided up to 34 data

**Table 1.** Variance Reduction by Period for Regionalized Model

| Wave Period (s) | Number of Rays | Velocity Rank | Phase Variance Reduction (%) | Events |
|---|---|---|---|---|
| 15 | 477 | 2.92 | 98.31 | 22 |
| 18 | 1148 | 2.97 | 99.39 | 43 |
| 20 | 1216 | 2.97 | 99.54 | 46 |
| 22.5 | 1610 | 2.98 | 99.75 | 56 |
| 25 | 1703 | 2.97 | 99.77 | 60 |
| 27.5 | 1682 | 2.97 | 99.85 | 63 |
| 30 | 1706 | 2.96 | 99.82 | 64 |
| 35 | 1638 | 2.95 | 99.85 | 59 |
| 40 | 1539 | 2.93 | 99.83 | 51 |
| 45 | 1948 | 2.91 | 99.65 | 68 |
| 50 | 2098 | 2.89 | 99.49 | 69 |
| 66 | 183 | 2.72 | 99.60 | 64 |
| 75 | 1418 | 2.67 | 99.60 | 53 |
| 90 | 1082 | 2.35 | 99.45 | 38 |
| 110 | 750 | 1.88 | 99.69 | 28 |
| 125 | 481 | 1.50 | 99.80 | 18 |
| 150 | 420 | 0.75 | 99.58 | 16 |

associated with 17 periods with one real and one imaginary component at each band-pass period.

## 3. Method

### 3.1. Phase Velocity Measurement With Two Plane Wave Approximation

[6] To estimate phase velocity, we used a technique developed by *Forsyth and Li* [2005] which accounts for simple multipathing effects, allowing shorter period Rayleigh waves to be reliably measured. This improves resolution, and has been used successfully in many studies [*Forsyth et al.*, 1998b; *Li et al.*, 2002, 2003; *Weeraratne et al.*, 2003; *Fischer et al.*, 2005]. For each band-pass period, the real and imaginary Fourier components were inverted for phase velocity, using the following steps:

[7] 1. The effects of wave multipathing are estimated by parameterizing the incoming waveform as two interfering plane waves. The six parameters associated with these two plane waves are constrained using a simulated annealing search [*Forsyth et al.*, 1998b; *Li et al.*, 2002, 2003; *Weeraratne et al.*, 2003; *Fischer et al.*, 2005].

[8] 2. Using the plane wave parameters derived in step 1 and a starting phase velocity model (discussed below), the data are iteratively inverted for updates to the starting model using

$$\Delta \mathbf{m} = \left(\mathbf{G}^{\mathbf{T}}\mathbf{C}_{\mathbf{dd}}^{-\mathbf{1}}\mathbf{G} + \mathbf{C}_{\mathbf{mm}}^{-\mathbf{1}}\right)^{-\mathbf{1}}\left(\mathbf{G}^{\mathbf{T}}\mathbf{C}_{\mathbf{dd}}^{-\mathbf{1}}\Delta \mathbf{d} - \mathbf{C}_{\mathbf{mm}}^{-\mathbf{1}}[\mathbf{m} - \mathbf{m_o}]\right), \quad (1)$$

where $\mathbf{G}$ is the matrix of partial derivatives, $\mathbf{C_{mm}}$ and $\mathbf{C_{dd}}$ are the a priori model and data covariance matrices, $\Delta\mathbf{d}$ is the difference between the observed and predicted Fourier coefficients, $\mathbf{m_o}$ is the original starting model, and $\mathbf{m}$ is the current model [*Tarantola and Valette*, 1982]. With each iteration, high misfit events are downweighted to minimize the effects of Rayleigh waves that are too multipathed to be fit by the two-plane wave approximation [*Forsyth and Li*, 2005].

[9] Ideally, the data would be sufficient to produce a fully resolved two-dimensional model of phase velocity variations for each wave period. However, similar to most teleseismic tomography, there were insufficient data to produce a unique two dimensional phase velocity map [*Menke*, 1989]. Similar to previous studies using the two-plane wave technique, we take a conservative approach to this problem and seek to find the simplest model parameterization that fits the data [*Forsyth et al.*, 1998a; *Li et al.*, 2002; *Li and Detrick*, 2003; *Li et al.*, 2003; *Weeraratne et al.*, 2003; *Fischer et al.*, 2005; *Forsyth and Li*, 2005; *Li and Detrick*, 2006]. To accomplish this, three sets of phase velocity inversions were conducted, starting with a uniform phase velocity inversion, proceeding to a regionalized phase velocity, and ending with a two-dimensional phase velocity inversion. The regionalization domains are defined based on teleseismic *P* and *S* body wave tomograms [*Schutt and Humphreys*, 2004; *Yuan and Dueker*, 2005; *Waite et al.*, 2006]. Our most important choice is the width of the hot spot track (Figure 1). The body-wave tomograms constrain the low velocity body beneath the hot spot track above 100 km depth to be 80–120 km wide. But, in the 100–200 km depth range the width of the low velocity anomaly varies between 150 and 200 km. Given that our resolution kernels have little sensitivity below 120 km depth, we have chosen to fix the width of the regionalized hot spot track width to 110 km.

[10] The uniform model is used as initial starting model (**m** in equation (1), above) for the next more complicated model. Specifically, the following three inversions are performed.

[11] 1. Invert Rayleigh wave observations for mean phase velocity at each wave period.

[12] 2. Use (1) as a starting model, and invert observations for mean phase velocity in each of the three tectonic regions: Basin and Range (BR), Wyoming Craton (WY), and Yellowstone hot spot track (YHT) (Figure 1).

[13] 3. Use (2) as a starting model and invert data for two-dimensional phase velocity maps. In these inversions, we use "fat ray" Gaussian approximations to the sensitivity kernels. Ray width is chosen such that 95% of the cross-sectional area falls within the first Fresnel zone [*Weeraratne et al.*, 2003; *Gudmundsson*, 1996].

[14] Thus, at each of the 17 data periods, three sets of inversions are performed with each inversion requiring two steps. Statistics for the inversion of 30 s waves are listed in Table 2. Note that because poorly fit events are downweighted, the variance reduction between models cannot be strictly compared [*Forsyth and Li*, 2005].

[15] Figure 3 shows the results of the regionalized phase velocity inversions. The data fit is excellent with 85–95% of the data variance being explained by the three region model (after poorly fit events are downweighted). This suggests that the regionalized velocity structure is a good approximation to the actual structure. To assess whether the mean phase velocity of the tectonic regions is uniquely resolved, the rank of the resolution matrix

$$\mathbf{R} = \left(\mathbf{G}^{\mathbf{T}}\mathbf{C}_{\mathbf{dd}}^{-\mathbf{1}}\mathbf{G} + \mathbf{C}_{\mathbf{mm}}^{-\mathbf{1}}\right)^{-\mathbf{1}}\mathbf{G}^{\mathbf{T}}\mathbf{C}_{\mathbf{dd}}^{-\mathbf{1}}\mathbf{G}, \quad (2)$$

is calculated (Figure 3c; variables are the same as in equation (1)). This value diminishes from a value of three for the shortest periods, implying that the mean phase

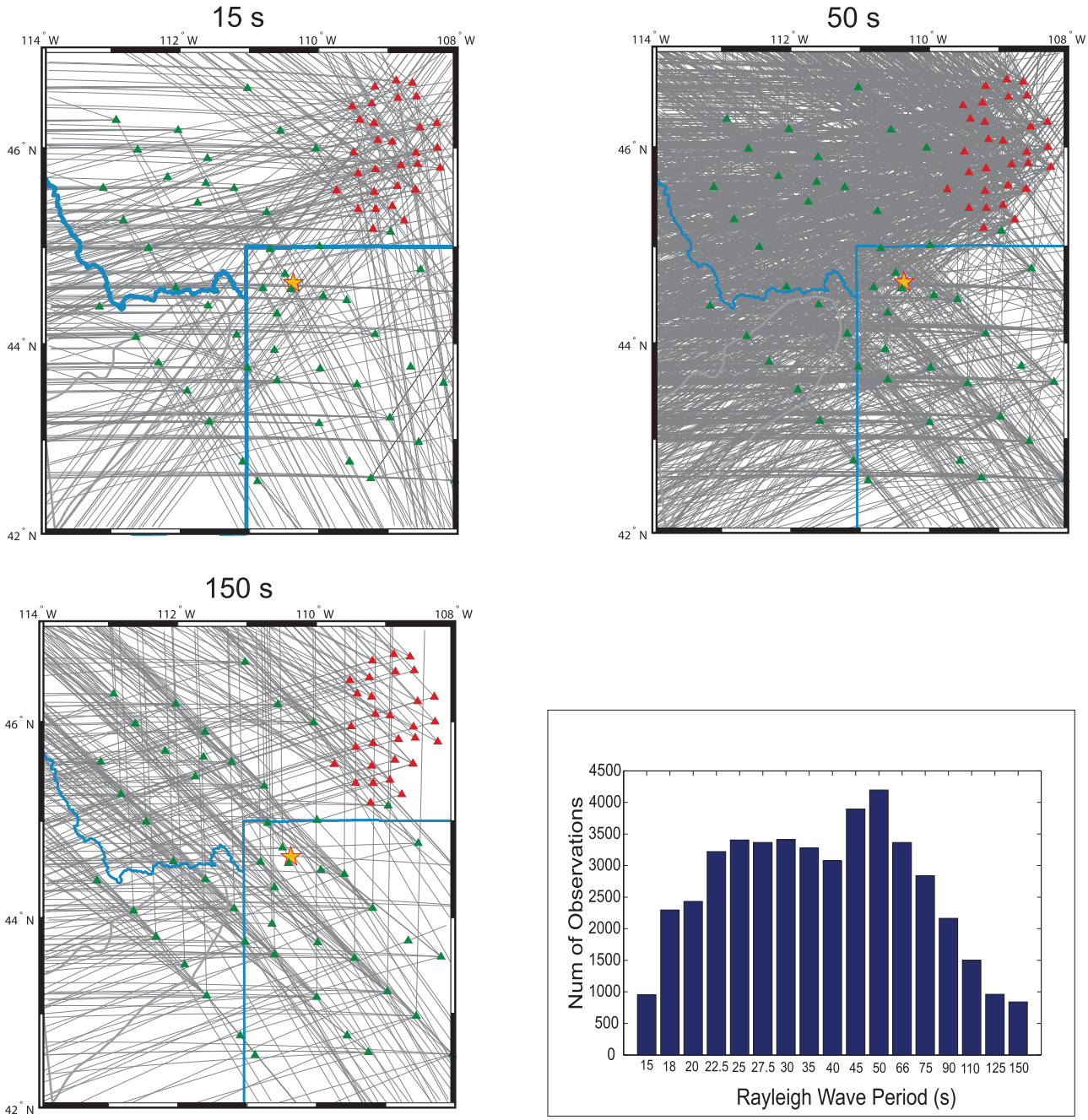


**Figure 2.** Station-event surface wave great circle paths used in the 150, 50, and 15 s inversions. Yellowstone and Billings stations are indicated by green and red triangles, respectively. Yellow star shows the Sour Creek volcanic dome as a proxy for the current location of the hot spot. The histogram shows observed data for each wave period. Data coverage is excellent for wave periods between 18 and 90 s.

velocity within each region is uniquely resolved, to less than one for the 150 s period. A unique regionalized phase velocity for the longest period waves cannot be resolved because of the relatively narrow width of the YHT and BR regions.

[16] Another way to assess the regionalized inversions robustness is to compare the results of the regionalized

**Table 2.** Phase Velocity Results at 30 s

| Model | Velocity Variations | Starting Model | Nobs | RMS Phase Misfit (s) | Total Variance Reduction (%) | Phase Variance Reduction (%) |
|---|---|---|---|---|---|---|
| 1 | constant | none | 3412 | 2.14 | 86.75 | 99.18% |
| 2 | regionalized | Model 1 | 3412 | 2.07 | 94.16 | 99.81% |
| 3 | 2-D | Model 1 | 3412 | 1.93 | 93.56 | 99.84% |
| 4 | 2-D | Model 2 | 3412 | 2.05 | 93.72 | 99.82% |

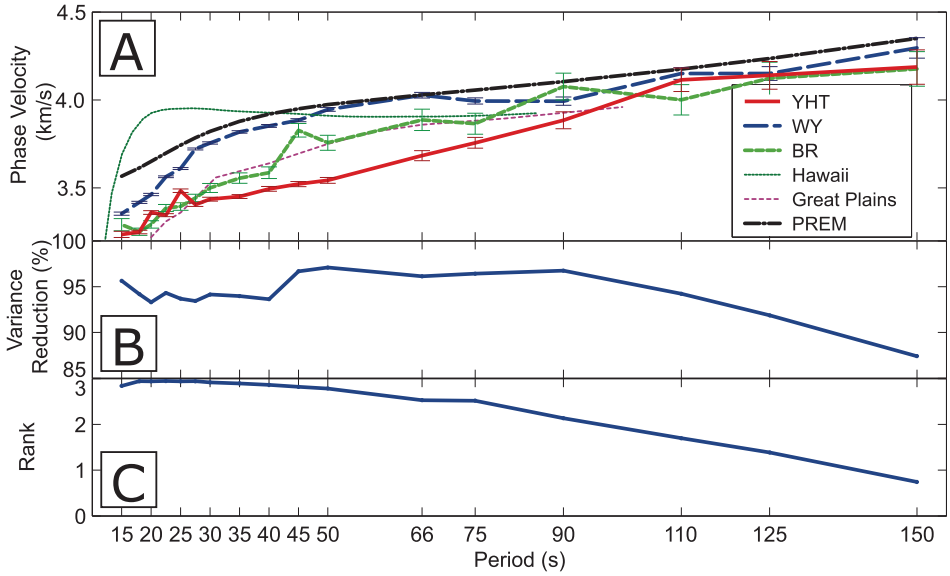


**Figure 3.** Regionalized phase velocity results. (a) Regionalized phase velocities compared to Hawaii [*Priestley and Tilmann*, 1999], PREM [*Dziewonski and Anderson*, 1981], and the Colorado Great Plains [*Li et al.*, 2002]. (b) Phase variance reduction after down-weighting poorly fit events. (c) Model resolution matrix rank at each period for the three region inversion. When the rank is greater than two, the mean phase velocities of the regions are independently resolved. At periods >75 s, the phase velocities between the regions cannot be independently resolved.

inversion with the two dimensional inversions (Figure 4). For wave periods >50 s, no significant perturbations to the regionalized phase velocities are required to fit the data. This observation implies that it is sufficient to characterize the velocity structure in terms of our three tectonic regions. One can also see the effect of the regionalized starting model on the 2-D inversion results by comparing inversions performed using the regionalized starting model (model 4 in Table 2) to those that did not use the regionalized starting model (model 3) (Figure 5). The effect of the regionalized starting model is evidenced by the continuity of the low velocities along the hot spot track. Correspondingly, the nonregionalized model does not show this hot spot track continuity. Our preference for the regionalized model is based upon two reasons. First, the body wave tomograms show that this is an accurate regionalization: in particular the 110 km width of the hot spot track domain is well constrained by the body wave tomograms. Second, comparisons of the variance reductions between the three differently parameterized models (three velocity profile fit and the 2-D nonregionalized and regionalized starting model images) shows that all of them provide comparable fits to the data (Table 2).

[17] It might be expected that the strong velocity variations beneath our study area would cause some events to be poorly modeled by the two plane wave approximation to the incoming wavefield. As previously stated, strongly multipathed events are downweighted during the inversion. We note that the two plane wave technique has been used successfully at locations with strong velocity variations, such as Tanzania and the East Pacific Rise [*Forsyth et al.*, 1998b; *Weeraratne et al.*, 2003]. Examination of the well-fit events with a phase RMS misfit <3 s shows that no systematic misfit exists (Figure 6; Table 3). As expected, the wavefield parameters show increased scattering at shorter periods. For instance, the mean azimuthal anomaly (with respect to the great circle path) of the largest of the two plane waves decreases with increasing period. In addition, the amplitude ratio of the smaller plane wave to the larger plane wave also decreases with increasing period. Furthermore, the scatter of the primary wave azimuthal anomalies also decreases with increasing period. If the large mantle velocity anomaly is causing unusual behavior in the two plane wave fits, this would be expected to occur at the periods most sensitive to the depth of the anomaly, namely the 30–66 s period waves. Given that no distinctive increase in misfits occurs for this period range, we expect the main conclusions of the paper are not sensitive to strongly multipathed waves.

### 3.2. Effects of Azimuthal Anisotropy

[18] SKS phase shear-wave splitting measurements find a nearly uniform anisotropy field, having a mean horizontal fast symmetry direction of N43°E, with a mean split time of ~1.2 s [*Waite et al.*, 2005]. To assess the effect of azimuthal anisotropy on our phase velocity maps, $\cos(2\theta)$ and $\sin(2\theta)$ velocity terms, in which $\theta$ represents azimuth, are added to the model vector [*Montagner et al.*, 2000]. We then invert for isotropic phase velocity variations and the mean anisotropy magnitude and orientation at each period. The resulting phase velocity curves are very similar to the pure isotropic profiles (Figure 7). This result suggests that the regionalized isotropic phase velocity results are not significantly biased by velocity anisotropy.

### 3.3. Inversions of Phase Velocity for Regionalized Shear Wave Velocity Structure

[19] The regionalized phase velocity curves were used as data to invert for regionalized shear wave velocity profiles. This inversion was done iteratively by solving for perturba-

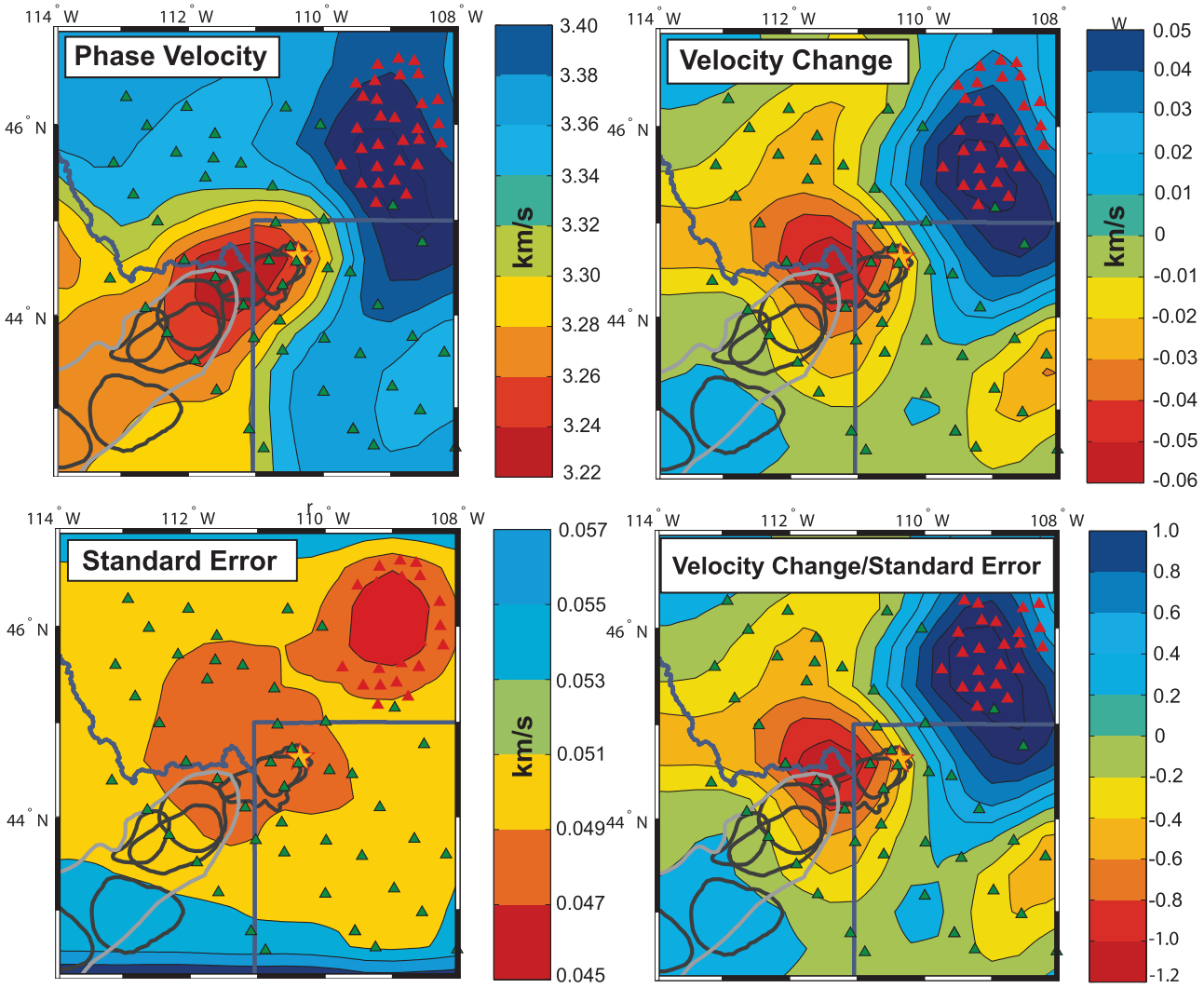


**Figure 4.** Two-dimensional phase velocity inversion of 15 s period waves. Yellowstone array stations are green triangles and Billing array stations are red triangles. Location of the Yellowstone hot spot is given by the yellow star. The top left-hand plot shows the phase velocity map. Top right-hand plot is the change from the starting model (the regionalized phase velocities shown in Figure 2). Bottom left plot is the standard error of the calculated phase velocities. Bottom right plot is the velocity change divided by the standard error which is proportional to velocity anomaly significance.

tions to an initially assumed $V_S$ model (equation (1)). Several starting velocity models based on previous observations were tested [*Greensfelder and Kovach*, 1982; *Priestley and Orcutt*, 1982; *Gorman et al.*, 2002]. In the end, a simple starting model was chosen that was the mean of the previous observations from the different regions. This starting model has a 42-km-thick three-layer crust, and a sub-Moho $V_S$ of 4.16 km/s (equivalent to a $V_P$ of 7.5 km/s for a $V_P/V_S$ value of 1.8) based on receiver function and previous refraction constraints for the YHT [*Sparlin et al.*, 1982; *Peng and Humphreys*, 1998, *Yuan et al.*, 2006, *Stachnik and Dueker*, 2006]. Below the Moho, $V_S$ was linearly increased from 4.16 km/s to match the $V_{SV}$ of PREM at 200 km depth [*Dziewonski and Anderson*, 1981]. The $V_P$ profile was generated using PREM $V_P/V_{SV}$ values [*Dziewonski and Anderson*, 1981].

[20] On the basis of the initial $V_P$ and $V_S$ structure, data kernels $\partial c/\partial V_S$ (T, z) and $\partial c/\partial V_P$ (T, z) were calculated where c is phase velocity, T is wave period, and z is depth (Figure 8) [*Weeraratne et al.*, 2003]. Density effects on phase velocity have an insignificant effect and were fixed to nominal values [*Weeraratne et al.*, 2003]. The *S-P* wave velocity perturbation scaling ($dV_S/dV_P$) was assumed to be 1.2, appropriate for the near solidus conditions of the YHT [*Cammarano et al.*, 2003; *Schutt and Lesher*, 2006].

[21] The observed phase velocity maps were inverted iteratively for $V_S$ structure with the recalculation of the data kernels between iterations. The iteration was repeated until velocity updates changed <0.001 km/s. The least squares inversion was regularized using diagonal damping. The approximate "elbow" value of the damping parameter was 25 $s^{-2}$, and the best tradeoff between resolution and variance (Figure 9). For consistency, the same damping value was used for the regionalized BR and WY inversions, although this makes these inversions slightly underdamped (Figure 9). The rank of the resolution matrix for the

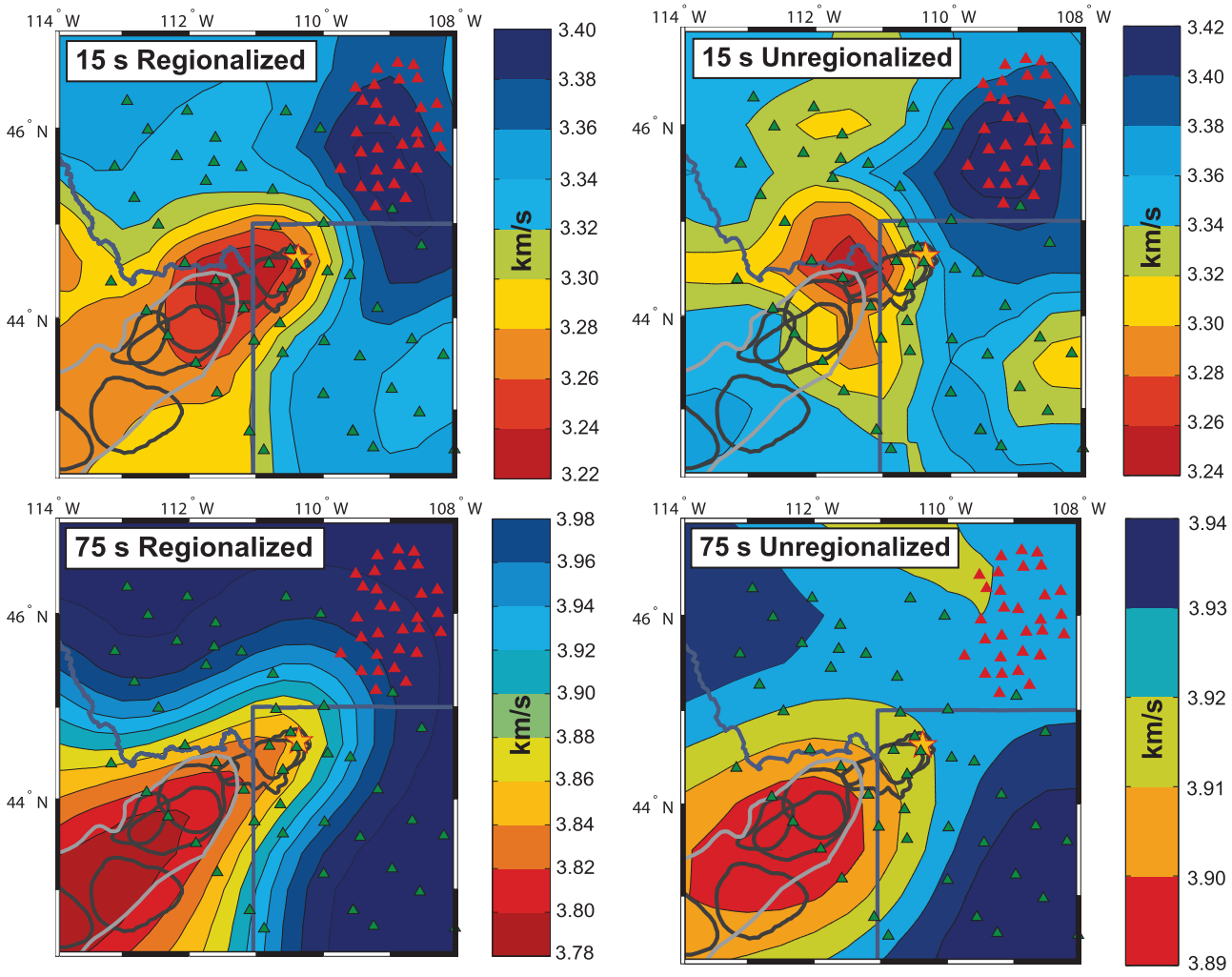


**Figure 5.** Effect of using a regionalized starting model on 2-D phase velocity inversion, for 15 and 75 s waves. Left column of figures are 2-D inversion results where the regionalized phase velocity structure (Figure 3) was used as a starting point. Right column of figures are the 2-D inversion results with a uniform starting model.

regionalized $V_S$ inversions varies from 3.7 for the Wyoming craton region to 2.1 for the Basin and Range region. As expected, the resolution diminishes with depth (Figure 10). Noteworthy is that our Rayleigh wave data set cannot resolve the midcrustal basalt sill beneath the eastern Snake River Plain [*Peng and Humphreys*, 1998], the bottom of the low velocity plume layer, or the plume conduit.

### 3.4. Inversions of Phase Velocity for 3-D Shear Wave Velocity Structure

[22] Because inversions of phase velocity maps for $V_S$ are quite sensitive to crustal velocity and thickness variations (Figure 8), it is important to incorporate a priori information on crustal thickness. We have used measurements of the time difference between the direct *P* arrival and the Moho converted $P_m$s arrival (hereafter called the $P_m$s time) from receiver functions as crustal thickness constraints [*Yuan et al.*, 2006]. These $P_m$s times were spatially averaged using a Gaussian half-width of 40 km to create a smoothed 2-D map (Figure 11). The coherent pattern of $P_m$s time variations varies by 2.4 s due to crustal thickness variations between 38 and 54 km [*Yuan et al.*, 2006]. In addition, receiver function reverberation analysis finds a mean crustal $V_P/V_S$ value of 1.78 [*Yuan et al.*, 2006].

[23] The $P_m$s times are incorporated into our velocity inversions as constraints. For each surface grid point, the $V_S$ and $V_P$ starting profiles ($V_S$ and $V_P$ as a function of depth for that grid point) used in the regionalized $V_S$ inversion were modified by adjusting the thickness of the lower crustal layer to match the observed $P_m$s times. Using these modified $V_S$ and $V_P$ profiles, data kernels were generated to invert the observed 2-D phase velocity maps (Figure 4) for an updated $V_S$ structure. The updated $V_S$ structure is then used with the $P_m$s time constraints to estimate a new crustal thickness. This process was iterated three times until the $V_S$ and $V_P$ profiles matched the observed $P_{mS}$ times within their error bars. Synthetic tests show that the crustal thickness and mean crustal velocity can be resolved within a few percent of their true values. The bootstrap estimated $P_m$s time errors are ±0.2 s and the $V_P/V_S$ errors are ±0.04. Given these uncertainties, crustal thicknesses are accurate to ±3 km, and the mean crustal $V_S$ is accurate to ±0.1 km/s.

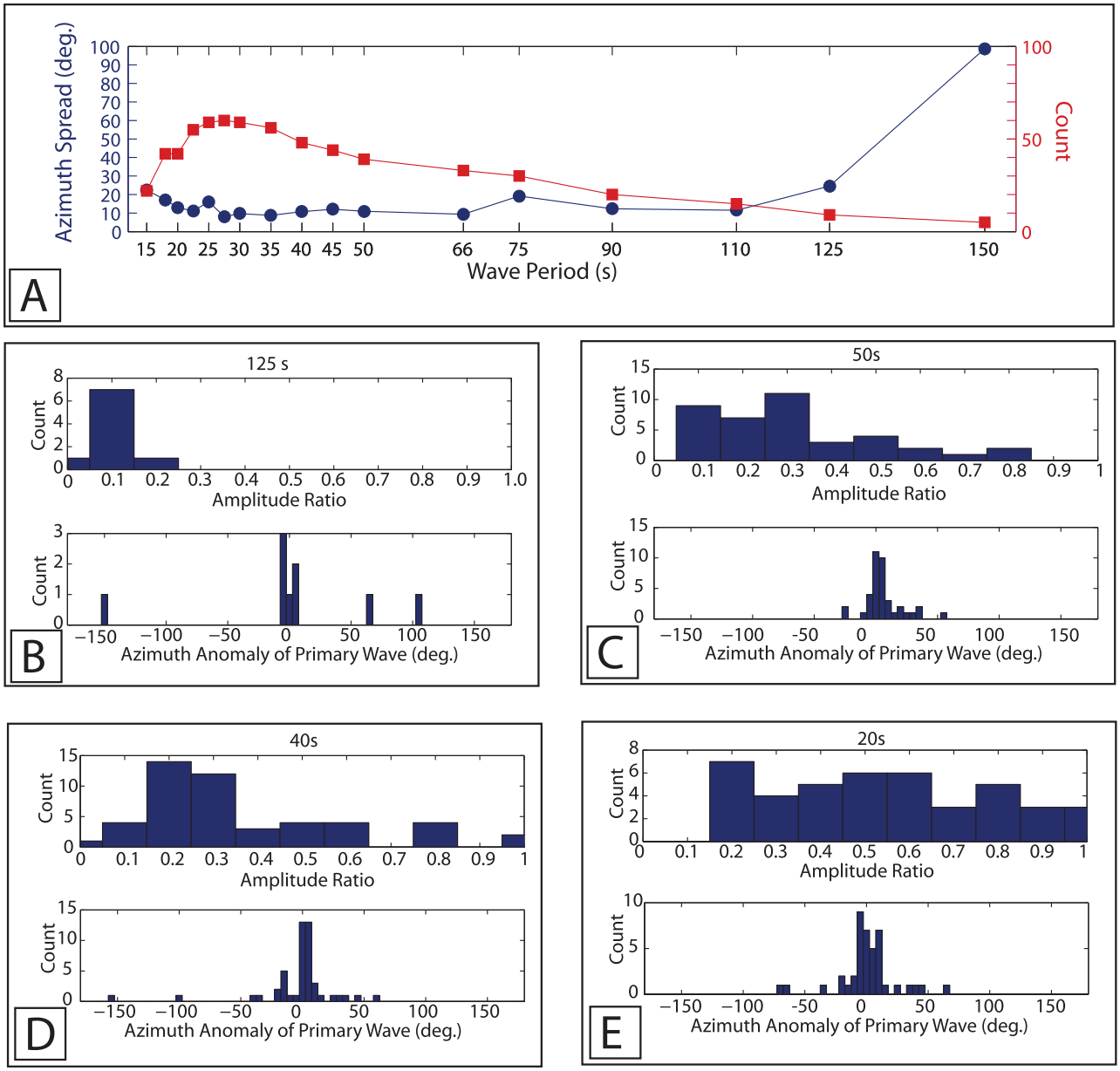


**Figure 6.** Two plane wave parameters. (a) Azimuth spread (blue) and number of events with a phase root-mean-square misfit of <3 s (red). The azimuth spread is the interquartile range of the azimuth of the primary waves. (b)–(e) Histograms of amplitude ratio and azimuth anomaly, the mean deviation of the primary wave from the great circle path, for 125, 50, 40, and 20 s waves, respectively. The amplitude ratio subplots are the ratios between the smaller (secondary) and larger (primary) amplitude plane waves.

[24] Vertical resolution of the velocity inversions can be estimated from the rank of the resolution matrices (Figure 12). Resolution at the depth of the low velocity channel (~70 km) in the mantle is ±20–30 km and diminishes with depth [*Weereratne et al.*, 2003]. Horizontal resolution varies with depth: within the crust horizontal resolution is ~40 km and at 150 km depth is 150 km. The 2-D phase velocity models produced with regionalized and nonregionalized starting model show how the regionalization affects the lateral resolution of the surface waves (Figure 5). In general, the horizontal and vertical 2-D resolution is sufficient to determine crustal velocity variations and the horizontal extent and velocity of the plume layer.

## 4. Results

[25] Crustal thickness ranges from 38 to 54 km with the thinnest crust beneath the Montana Basin and Range province and thickest crust beneath the Wyoming Craton (Figure 13a). Average crustal S-wave velocity varies by 11% with low velocities in the BR and YHT regions ($V_S$ = 3.4, $V_P$ = 6.0) and highest velocities in the northeast quadrant of the image ($V_S$ = 3.8, $V_P$ = 6.6; Figure 13b). These mean crustal velocities are consistent with other

**Table 3.** Statistics From Two Plane Wave Fits[a]

| Wave Period (s) | N | Median Amplitude Ratio | Median Azimuthal Anomaly (deg) | Azimuthal Spread (deg) |
|---|---|---|---|---|
| 150 | 5 | 0.096 | 5.617 | 98.774 |
| 125 | 9 | 0.103 | 5.874 | 24.56 |
| 110 | 15 | 0.143 | 3.282 | 11.468 |
| 90 | 20 | 0.222 | 6.113 | 12.311 |
| 75 | 30 | 0.192 | 5.026 | 19.222 |
| 66 | 33 | 0.299 | 3.84 | 9.316 |
| 50 | 39 | 0.296 | 4.17 | 10.917 |
| 45 | 44 | 0.279 | 5.563 | 12.052 |
| 40 | 48 | 0.28 | 4.839 | 10.786 |
| 35 | 56 | 0.36 | 6.915 | 8.74 |
| 30 | 59 | 0.382 | 3.678 | 9.725 |
| 27.5 | 60 | 0.362 | 4.146 | 8.128 |
| 25 | 59 | 0.408 | 7.398 | 16.052 |
| 22.5 | 55 | 0.454 | 6.434 | 11.164 |
| 20 | 42 | 0.518 | 7.332 | 12.925 |
| 18 | 42 | 0.501 | 7.596 | 17.109 |
| 15 | 22 | 0.638 | 14.544 | 22.402 |

[a]See Figure 6 caption for explanation of columns.

studies in the region [*Gorman et al.*, 2002; *Zhou and Stump*, 2004; *Zeiler et al.*, 2005].

[26] Beneath the YHT, a profound low velocity zone with a velocity minimum of 3.8 km/s at 80 km depth is imaged (Figure 11 and 13) which is 7% lower than the adjacent 4.1 km/s mantle. The 100 km width of the hot spot track anomaly imaged by the body wave tomograms [*Saltzer and Humphreys*, 1997; *Schutt and Humphreys*, 2004; *Yuan and Dueker*, 2005; *Waite et al.*, 2006] is similar to the 80 km width of the eastern Snake River Plain. The halo of average velocities (yellow colors in Figure 13c) around the hot spot track is caused by inversion regularization, and the actual velocity transition is sharper as resolved by body wave tomography. It is notable that our velocity model is consistent with plume material only residing beneath the 100 km wide eastern Snake River Plain, compared to the much broader "tectonic parabola" which is based on current-faulting and paleofaulting rates [e.g., *Anders and Sleep*, 1992]. Below 100 km depth, the surface wave data cannot uniquely resolve the width of the plume mantle. Indeed, the width of the deep low velocity zone is defined by the regionalization, derived from the body wave tomography [*Yuan and Dueker*, 2005; *Waite et al.*, 2006].

[27] The YHT low velocity anomaly extends to about 120 km depth before intersecting the shear velocity predicted for a 1320°C adiabatic mantle [*Cammarano et al.*, 2003; *Faul and Jackson*, 2005; *Stixrude and Lithgow-Bertelloni*, 2005]. However, the base of the low velocity plume layer is not well resolved due to declining resolution with depth. Noteworthy is that no perturbations of our starting model are required below 140 km depth (Figure 10).

## 5. Discussion

[28] The 4.2 km/s velocity at 95 km depth beneath the Wyoming craton to the east of the hot spot (Figures 13d and 13e) is similar to the shear velocity for 4–20 Ma oceanic profiles [*Nishimura and Forsyth*, 1989]. This suggests that below 90 km the Wyoming province mantle temperature is consistent with a nominal mantle adiabat [*Faul and Jackson*, 2005]. Yet, xenoliths from the Eocene William Kimberlite in east Montana suggests a 170 km thick lithosphere existed here 50 Ma ago [*Carlson et al.*, 1999]. To reconcile this thick Eocene-age lithosphere with the thinner modern day Wyoming lithosphere, we speculate that the Laramide-age slab hydrated the lithosphere [*Humphreys et al.*, 2003] to enable subsequent post-Laramide convective destabilization and lithospheric thinning. This potential convective thinning may have been initiated or accelerated by the nearby Yellowstone plume. However, we reiterate that no plume material extends significantly beyond the confines of the YHT, albeit the entrainment of ambient mantle certainly does extend outward [*Yuan and Dueker*, 2005; *Waite et al.*, 2006].

[29] The 3.8 km/s velocity minimum at 80 km under the YHT compares to minimum shear velocity of 4.0 km/s for the Hawaii to Oahu path [*Priestley and Tilmann*, 1999] and 3.8 km/s in the western arm of the East Africa Rift [*Weeraratne et al.*, 2003]. Thus, the YHT uppermost mantle is one of the lowest velocity uppermost mantle regions on the Earth.

[30] Possible causes of the low mantle velocity are many: melt porosity, mantle hydration, small grain sizes, or increased temperature [*Karato*, 1993; *Karato et al.*, 1998; *Kreutzmann et al.*, 2004; *Faul and Jackson*, 2005]. If equilibrium melt porosity along the YHT is ~0.2% [*McKenzie*, 1984], then melt velocity scaling relationships

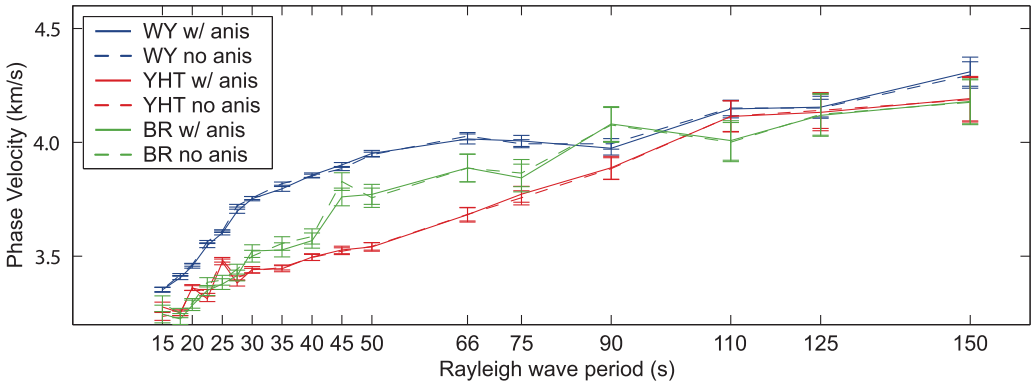


**Figure 7.** Isotropic versus anisotropic phase velocity inversion results for regionalized structure. Solid lines with one-sigma error bars are phase velocity results from anisotropic inversion, and dashed lines are phase velocity results as shown in Figure 3.

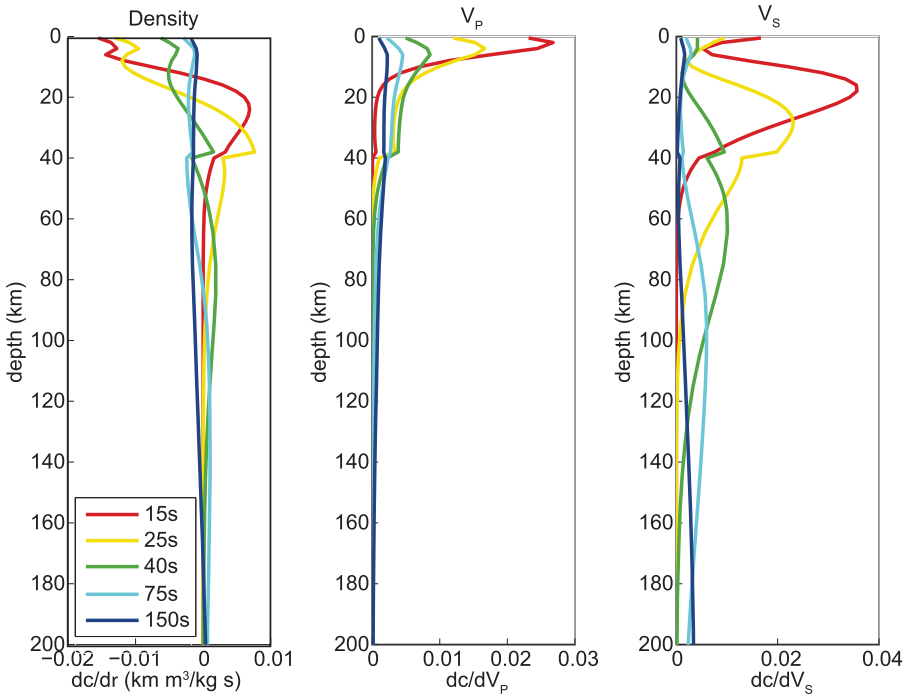


**Figure 8.** Data sensitivity kernels for density, shear, and compressional wave variations for 15, 25, 40, 75, and 150 s Rayleigh waves. Our starting velocity model with a 40 km thick crust is used for these kernels.

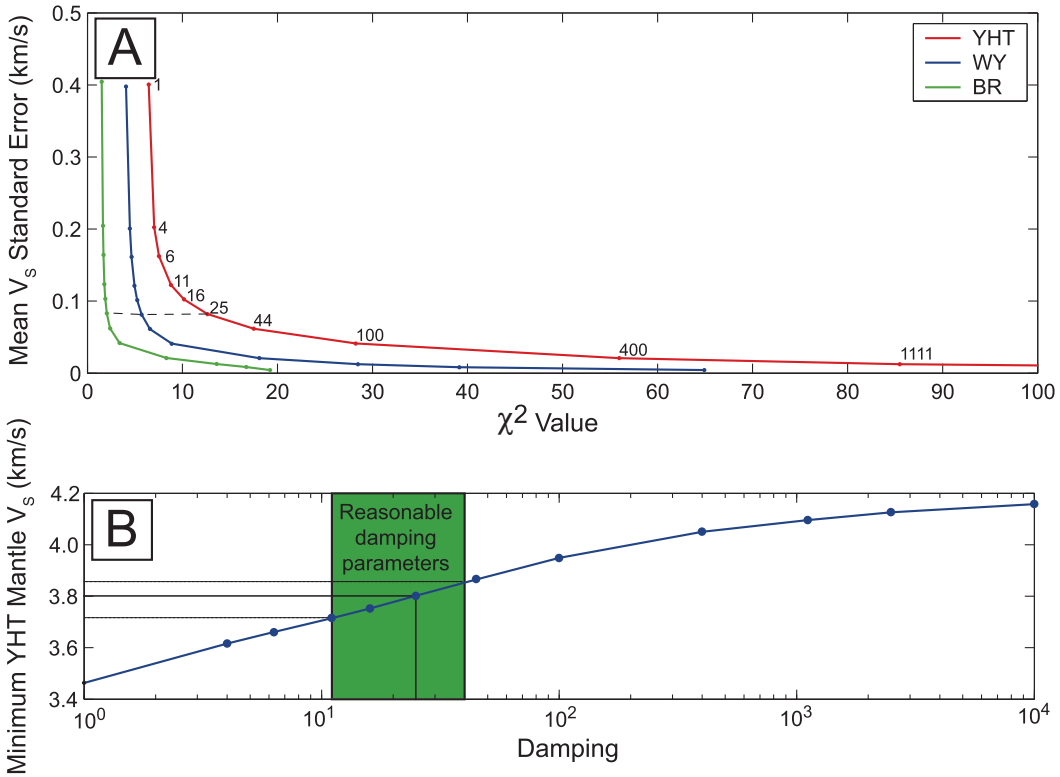


**Figure 9.** Estimation of best inverse problem damping value. (a) Inversion trade-off curves. The chi-squared value is plotted with respect to the mean shear velocity error (from 0 to 200 km depth) for the three regionalized shear velocity inversions. The numbers along the red line are the damping values. The dashed line indicate the damping value used. (b) Minimum YHT mantle $V_S$ as a function of damping values. The green area shows the estimated range of reasonable damping values and their effect on minimum YHT mantle velocity. The black line is the minimum $V_S$ for a 25 $s^{-2}$ damping, and dashed lines indicate rough error bounds. These error bounds are reflected in the 0.2 km/s velocity error bounds used in the text.

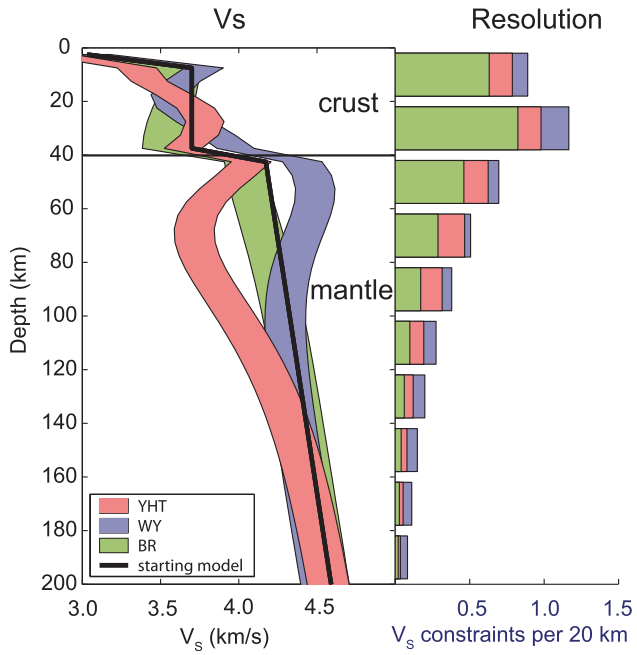


**Figure 10.** Regionalized S-wave velocity profiles and depth resolution. (a) The S-wave velocity profiles. Standard error of these profiles is shown by the width of the bands [*Weereratne et al.*, 2003]. The black line is the starting velocity structure. (b) Sum of the diagonal elements of the resolution matrix for 20 km wide depth bins. This shows that the Wyoming Craton and Yellowstone hot spot track structure is well resolved above 100 km.

[*Hammond and Humphreys*, 2000; *Kreutzmann et al.*, 2004] suggest the shear velocity reduction will be less than 1.5%.

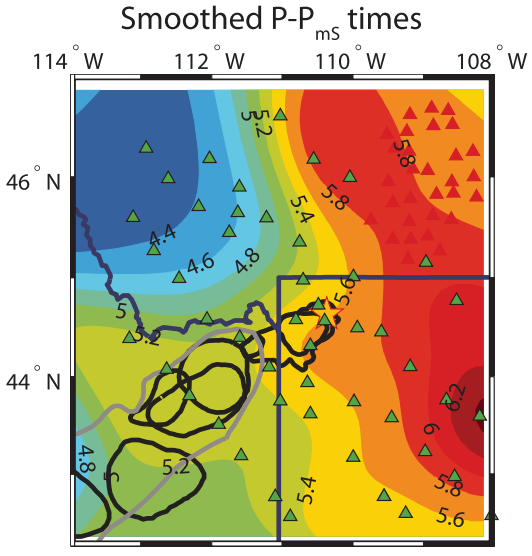


**Figure 11.** Arrival time difference between direct *P* waves and *P*-to-*S* wave conversions from the Moho determined from the receiver function study of *Yuan et al.* [2006]. The mean times are averaged for each station and then laterally smoothed with a 40 km half-width Gaussian.

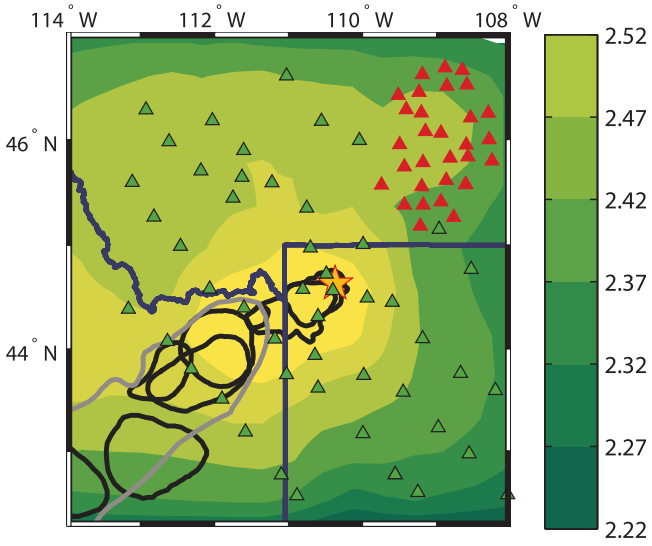


**Figure 12.** Map of model resolution matrix rank from inversions for three-dimensional velocity structure.

Water content probably does not lower the mean plume layer velocity because the majority of the low-velocity volume imaged under the YHT has had significant amounts of melt extracted [*Perkins and Nash*, 2002], which would dehydrate the matrix.

[31] Assuming significant velocity effects from melt porosity and hydration can be ruled out, this leaves variations in temperature [*Karato*, 1993; *Godey et al.*, 2004; *Faul and Jackson*, 2005] and grain size [*Faul and Jackson*, 2005] as the primary cause of the low velocities. While a future paper will detail these calculations, a robust statement is that our lowest mantle velocities of 3.8 km/s require a mantle >50° warmer than a 1320°C potential temperature mantle with high confidence [*Dueker et al.*, 2004].

[32] The narrow width of the plume track (100–200 km width) found by the tomographic body wave velocity images [e.g., *Yuan and Dueker*, 2005] and, consistent with this paper's findings, in tandem with lack of parabolic asthenospheric flow perturbations found by the SKS analysis [*Waite et al.*, 2005], requires that the Yellowstone plume must have a small buoyancy flux as previous topographic analysis suggests [*Sleep*, 1990]. Isostatic topography modeling suggests a maximum plume excess temperature of 200°C (with fairly large errors) [*Schutt and Humphreys*, 2004]. A 200°C thermal anomaly would have plume material that is <31 kg/m$^3$ lighter than surrounding mantle [*Schutt and Lesher*, 2006]. Assuming this buoyancy anomaly is distributed in a 60 km thick layer (60–120 km depth range) under the 80 km wide YHT, and using the North American absolute plate motion rate of 2.1 cm/a [*Gripp and Gordon*, 2002], a buoyancy flux of <0.1 Mg/s is calculated. This model assumes the mean upwelling rate of the Yellowstone plume is the same as the plate motion, based on the observation that there is no clear parabolic-like spreading of the plume. This contrasts with a previous estimation of 4.8 Mg/s from modeling dynamic elevation effects [*Lowry et al.*, 2000] and a ~9 Mg/s buoyancy flux for Hawaii [*Sleep*, 1990].

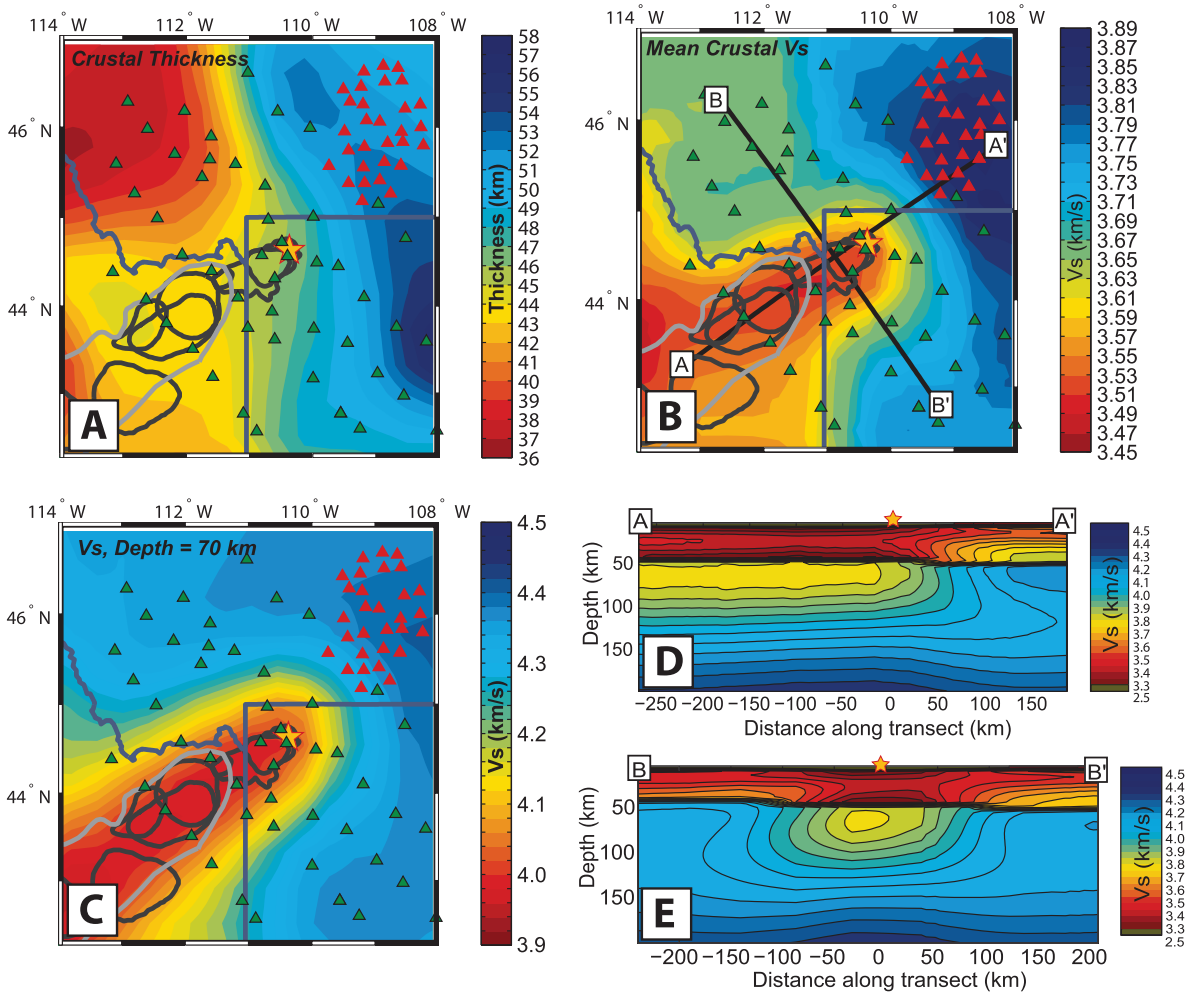


**Figure 13.** Three-dimensional shear wave velocity image. (a) Crustal thickness found by joint inversion of phase velocity maps and Moho $P_{mS}$ times. (b) Mean crustal shear wave velocity. (c) Map-view of velocity at 70 km depth. (d)–(e) Cross-sections A-A′ and B-B′ through the current location of the hot spot at Yellowstone Park. The yellow star denotes the current hot spot location and the gray lines outline the YHT calderas.

[33] Although the plume is clearly imaged to extend into the transition zone [*Yuan and Dueker*, 2005; *Waite et al.*, 2006], global tomographic images shows no plume extending into the lower mantle [*Montelli et al.*, 2004, 2006]. This suggests Yellowstone is an upper mantle plume which has either detached from the core mantle boundary or nucleated from an uppermost lower mantle low viscosity layer [*Cserepes and Yuen*, 2000].

[34] A speculative possibility for the life cycle of the Yellowstone plume is that the plume was nucleated at the CMB due to the influence of the sinking Farallon slab. The slab has primarily subducted to the east of Yellowstone, and in at least one convection model, the slab turns over on itself near the core mantle boundary [*Tan et al.*, 2002]. Downward flow from a slab has been shown to thin the lower thermal boundary layer under the slab, and thicken it outboard of the slab flow direction [*Tan et al.*, 2002]. This thickened thermal boundary layer could serve as a stimulus to nucleate the plume. As the plume head nears the base of the lithosphere, preexisting lithospheric thickness gradients may channel the plume flow to produce the voluminous Columbia River and Steens basalt outpourings [*Jordan et al.*, 2004]. After this initial impact stage about 18–16 ma ago, the plume tail then begins to primarily melt the lithosphere [*Doe et al.*, 1982; *Menzies et al.*, 1983] to create the Yellowstone hot spot track.

[35] An additional finding is that the thick high velocity lower crust found within the Wyoming Craton is consistent with the 7.1 km/s lower crust found by the Deep Probe experiment [*Henstock et al.*, 1998; *Gorman et al.*, 2002]. The coincident 5–8 km increase in crustal thickness and 5% increase in shear velocity suggest this high-velocity layer thickens to the east. Assuming this high velocity layer is due to basalt emplacement, and the crust above this layer has an average 3.6 km/s shear velocity, the increase in velocity and thickness can be explained as an ancient magmatic underplate, whose thickness increases from 7 to 19 km. This suggests a large input of magma associated with either the 2.6 Ga Stillwater Complex [*McCallum*, 1996] or the 1.8 Ga magmatic event recorded by Montana mantle xenoliths [*Carlson et al.*, 1999].

## 6. Conclusion

[36] Measurements of fundamental mode Rayleigh waves show very low phase velocities along the Yellowstone hot spot track in the 30–60 s wave period band. Inversion for shear wave velocity structure resolves minimum mantle velocities of 3.8–3.9 km/s at 80 km depth beneath the hot spot track. These uppermost mantle velocities are among the lowest on the planet. Outside the hot spot track, asthenospheric mantle velocities are consistent with adiabatic mantle. We conclude that Yellowstone hot spot track mantle does not have enough water content nor melt porosity to produce the observed low velocities; hence, a significant temperature anomaly is required. This suggests the Yellowstone is hot with respect to adiabatic mantle. Combined with body wave tomograms that show a cylindrical low velocity feature extending into the transition zone, it is clear that Yellowstone is a thermal mantle plume, albeit a very weak one with no lower mantle extension.

[37] **Acknowledgments.** We thank two anonymous reviewers, one of the Associate Editors of JGR, and Editor J.C. Mutter for many helpful comments with the manuscript. We also wish to thank D. Forsyth for unselfishly sharing his surface wave code and for advice on how to use it, as well as D. Weeraratne, who also provided code and answered many questions. Data was provided by the IRIS DMC, whom we thank. We also thank the National Science Foundation for grants 0440432 and 0409538 and for an Individual Research and Development time provided to DS while working at the NSF.

## References

Anders, M. H., and N. H. Sleep (1992), Magmatism and extension: The thermal and mechanical effects of the Yellowstone hot spot, *J. Geophys. Res.*, *97*(B11), 15,379–15,393.

Armstrong, R. L., and W. P. Leeman (1975), K-Ar dating, Quaternary and Neogene volcanism of the Snake River Plain, Idaho, *Am J. Sci.*, *275*, 225–251.

Cammarano, F., S. Goes, P. Vacher, and D. Giardini (2003), Inferring upper-mantle temperatures from seismic velocities, *Phys. Earth Planet. Int.*, *138*(3–4), 197–222.

Carlson, R. W., A. J. Irving, and B. C. Hearn Jr. (1999), Chemical and isotopic systematics of peridotite xenoliths from the Williams Kimberlite, Montana: Clues to processes of lithosphere formation, modification and destruction, in *Proceedings of the VIIth International Kimberlite Conference*, vol. 1, edited by J. L. Gurney, M. D. Pascoe, and S. H. Richardson, Univ. of Cape Town, Rondebosch, South Africa.

Christiansen, R. L., and R. S. Yeats (1992), Post-Laramide geology of the U.S. Cordilleran region, in *The Geology of North America*, edited by B. C. Burchfiel, P. W. Lipman, and M. L. Zoback, pp. 261–406, Geol. Soc. of Am., Boulder, Colo.

Christiansen, R. L., G. R. Foulger, and J. R. Evans (2002), Upper-mantle origin of the Yellowstone hotspot, *Bull. Geol. Soc. Am.*, *114*(10), 1245–1256.

Cserepes, L., and D. A. Yuen (2000), On the possibility of a second kind of mantle plume, *Earth Planet. Sci. Lett.*, *183*(1–2), 61–71.

Doe, B. R., W. P. Leeman, R. L. Christiansen, and C. E. Hedge (1982), Lead and strontium isotopes and related trace elements as genetic tracers in the Upper Cenozoic rhyolite-basalt association of the Yellowstone Plateau volcanic field, *J. Geophys. Res.*, *87*(B6), 4785–4806.

Dueker, K. G., D. L. Schutt, H. Yuan, and D. Fee (2004), New seismic constraints for the Yellowstone hot spot, *Eos. Trans. AGU*, *85*(47), Fall Meet. Suppl., Abstract V51B-0554.

Dziewonski, A. M., and D. L. Anderson (1981), Preliminary reference Earth model, *Phys. Earth. Planet. Int.*, *25*(4), 297–356.

Faul, U. H., and H. R. Jackson (2005), The seismological signature of temperature and grain size variations in the upper mantle, *Earth Planet. Sci. Lett.*, *234*, 119–134.

Fee, D., and K. Dueker (2004), Mantle transition zone topography and structure beneath the Yellowstone hot spot, *Geophys. Res. Lett.*, *31*, L18603, doi:10.1029/2004GL020636.

Fischer, K. M., A. Li, D. W. Forsyth, and S.-H. Hung (2005), Imaging three-dimensional anisotropy with broadband seismometer arrays, in *Seismic Earth: Array Analysis of Broadband Seismograms*, *Geophys. Monogr. Ser.*, vol. 187, edited by A. Levander and G. Nolet, pp. 99–106, AGU, Washington, D.C.

Forsyth, D. W., and A. Li (2005), Array-analysis of two-dimensional variations in surface wave phase velocity and azimuthal anisotropy in the presence of multipathing interference., in *Seismic Earth: Array Analysis of Broadband Seismograms*, *Geophys. Monogr. Ser.*, vol. 187, edited by A. Levander and G. Nolet, pp. 81–98, AGU, Washington, D.C.

Forsyth, D. W., et al. (1998a), Imaging the deep seismic structure beneath a mid-ocean ridge; the MELT experiment, *Science*, *280*(5367), 1215–1218.

Forsyth, D. W., S. C. Webb, L. M. Dorman, and Y. Shen (1998b), Phase velocities of Rayleigh waves in the MELT experiment on the East Pacific Rise, *Science*, *280*(5367), 1235–1238.

Godey, S., F. Deschamps, J. Trampert, and R. Snieder (2004), Thermal and compositional anomalies beneath the North American continent, *J. Geophys. Res.*, *109*, B01308, doi:10.1029/2002JB002263.

Gorman, A. R., et al. (2002), Deep Probe; imaging the roots of western North America, in *The Lithoprobe Alberta Basement Transect (Le transect Lithoprobe du socle albertain)*, edited by M. Ross Gerald, pp. 375–398, Natl. Res. Council of Canada, Ottawa, Ontario, Canada.

Greensfelder, R. W., and R. L. Kovach (1982), Shear wave velocities and crustal structure of the eastern Snake River plain, Idaho, *J. Geophys. Res.*, *87*(4), 2643–2653.

Gripp, A. E., and R. G. Gordon (2002), Young tracks of hotspots and current plate velocities, *Geophys. J. Int.*, *150*(2), 321–361.

Gudmundsson, O. (1996), On the effect of diffraction on traveltime measurements, *Geophys. J. Int.*, *124*(1), 304–314.

Hamilton, W. B. (1989). Crustal geologic processes of the United States, in *Geophysical Framework of the Continental United States*, edited by L. C. Pakiser and W. D. Mooney, pp. 743–781, Geol. Soc. of Am., Boulder, Colo.

Hammond, W. C., and E. D. Humphreys (2000), Upper mantle seismic wave velocity: Effects of realistic partial melt geometries, *J. Geophys. Res.*, *105*(B5), 10,975–10,986.

Henstock, T. J., et al. (1998), Probing the Archean and Proterozoic lithosphere of western North America, *GSA Today*, *8*, 1–5.

Humphreys, E., and K. G. Dueker (1994), Western U.S. upper mantle structure, *J. Geophys. Res.*, *99*(B5), 9615–9634.

Humphreys, E., E. Erslev, T. Atwater, E. Hessler, K. Dueker, and G. L. Farmer (2003), How laramide-age hydration of North American Lithosphere by the Farallon Slab controlled subsequent activity in the Western United States, *Int. Geol. Rev.*, *45*(7), 524–544.

Jordan, B. T., A. L. Grunder, R. A. Duncan, and A. L. Deino (2004), Geochronology of age-progressive volcanism of the Oregon High Lava Plains: Implications for the plume interpretation of Yellowstone, *J. Geophys. Res.*, *109*, B10202, doi:10.1029/2003JB002776.

Karato, S. (1993), Importance of anelasticity in the interpretation of seismic tomography, *Geophys. Res. Lett.*, *20*(15), 1623–1626.

Karato, S., S. Zhang, M. E. Zimmerman, M. J. Daines, and D. L. Kohlstedt (1998), Experimental studies of shear deformation of mantle materials: Towards structural geology of the mantle, *Pure Appl. Geophys.*, *151*, 589–603.

Kreutzmann, H., H. Schmeling, H. Jung, T. Ruedas, G. Marquart, and I. T. Bjarnason (2004), Temperature and melting of a ridge-centered plume with application to Iceland. Part II: Predictions for electromagnetic and seismic observables, *Geophys. J. Int.*, *159*, 1097–1111.

Li, A., and R. S. Detrick (2003), Azimuthal anisotropy and phase velocity beneath Iceland: Implication for plume-ridge interaction, *Earth Planet. Sci. Lett.*, *214*(1–2), 153–165.

Li, A., and R. S. Detrick (2006), Seismic structure of Iceland from Rayleigh wave inversions and geodynamic implications, *Earth Planet. Sci. Lett.*, *241*(3–4), 901–912.

Li, A., D. W. Forsyth, and K. M. Fischer (2002), Evidence for shallow isostatic compensation of the southern Rocky Mountains from Rayleigh wave tomography, *Geology*, *30*(8), 683–686.

Li, A., D. W. Forsyth, and K. M. Fischer (2003), Shear velocity structure and azimuthal anisotropy beneath eastern North America from Rayleigh wave inversion, *J. Geophys. Res.*, *108*(B8), 2427, doi:10.1029/2002JB002273.

Lowry, A. R., N. M. Ribe, and R. B. Smith (2000), Dynamic elevation of the Cordillera, western United States, *J. Geophys. Res.*, *105*(B10), 23,371–23,390.

McCallum, I. S. (1996), The stillwater complex, in *Layered Intrusions*, edited by R. G. Cawthorn, pp. 441–483, Elsevier, Amsterdam.

McKenzie, D. M. (1984), The generation and compaction of partially molten rock, *J. Petrol.*, *25*, 713–765.

Menke, W. (1989), *Geophysical Data Analysis: Discrete Inverse Theory*, 289 pp., Academic, San Diego, Calif.

Menzies, M. A., W. P. Leeman, and C. J. Hawkesworth (1983), Isotope geochemistry of Cenozoic volcanic rocks reveals mantle heterogeneity below western USA, *Nature*, *303*(5914), 205–209.

Montagner, J.-P., D.-A. Griot-Pommera, and J. Lave (2000), How to relate body wave and surface wave anisotropy?, *J. Geophys. Res.*, *105*(8), 19,915–19,027.

Montelli, R., G. Nolet, G. Masters, F. A. Dahlen, and S. H. Hung (2004), Global P and PP traveltime tomography: Rays versus waves, *Geophys. J. Int.*, *158*(2), 637–654.

Montelli, R., G. Nolet, F. A. Dahlen, and G. Masters (2006), A catalogue of deep mantle plumes: New results from finite-frequency tomography, *Geochem. Geophys. Geosyst.*, *7*, Q11007, doi:10.1029/2006GC001248.

Morgan, L. A., D. J. Doherty, and W. P. Leeman (1984), Ignimbrites of the eastern Snake River Plain: evidence for major caldera-forming eruptions, *J. Geophys. Res.*, *89*(B10), 8665–8678.

Nishimura, C. E., and D. W. Forsyth (1989), The anisotropic structure of the upper mantle in the Pacific, *Geophys. J. Int.*, *96*, 203–229.

Peng, X., and E. D. Humphreys (1998), Crustal velocity structure across the eastern Snake River Plain and the Yellowstone swell, *J. Geophys. Res.*, *103*(B4), 7171–7186.

Perkins, M. E., and B. P. Nash (2002), Explosive silicic volcanism of the Yellowstone hotspot: The ash fall tuff record, *Geol. Soc. Am. Bull.*, *114*(3), 367–381.

Priestley, K. F., and J. Orcutt (1982), Extremal travel time inversion of explosion seismology data from the eastern Snake River plain, Idaho, *J. Geophys. Res.*, *87*(B4), 2634–2642.

Priestley, K. F., and F. J. Tilmann (1999), Shear-wave of the lithosphere above the Hawaiian hot spot from two-station Rayleigh wave phase velocity measurements, *Geophys. Res. Lett.*, *26*(10), 1493–1496.

Saltzer, R. L., and E. D. Humphreys (1997), Upper mantle *P* wave velocity structure of the eastern Snake River plain and its relationship to geodynamic models of the region, *J. Geophys. Res.*, *102*(B6), 11,829–11,841.

Schutt, D., and L. Humphreys (2004), *P* and *S* wave velocity and Vp/Vs in the wake of the Yellowstone hot spot, *J. Geophys. Res.*, *109*, B01305, doi:10.1029/2003JB002442.

Schutt, D. L., and C. E. Lesher (2006), The effects of melt depletion on the density and seismic velocity of garnet and spinel lherzolite, *J. Geophys. Res.*, *111*, B05401, doi:10.1029/2003JB002950.

Sleep, N. H. (1990), Hot spots and mantle plumes: Some phenomenology, *J. Geophys. Res.*, *95*(B5), 6715–6736.

Sparlin, M. A., L. W. Braile, and R. B. Smith (1982), Crustal structure of the eastern Snake River Plain from ray trace modeling of seismic refraction data, *J. Geophys. Res.*, *87*(B4), 2619–2633.

Stachnik, J. C., and K. Dueker (2006), Constraining Yellowstone magmatic processes beneath the eastern Snake River Plain from Rayleigh wave ambient noise, *Eos Trans. AGU*, *87*(52), Fall Meet. Suppl., Abstract S43A-1375.

Stixrude, L., and B. C. Lithgow-Bertelloni (2005), Mineralogy and elasticity of the oceanic upper mantle: Origin of the low-velocity zone, *J. Geophys. Res.*, *110*, B03204, doi:10.1029/2004JB002965.

Tan, E., M. Gurnis, and L. Han (2002), Slabs in the lower mantle and their modulation of plume formation, *Geochem. Geophys. Geosyst.*, *3*(11), 1067, doi:10.1029/2001GC000238.

Tarantola, A., and B. Valette (1982), Generalized nonlinear inverse problems solved using the least squares criterion, *Rev. Geophys.*, *20*(2), 219–232.

Waite, G., D. Schutt, and R. B. Smith (2005), Models of lithosphere and asthenosphere anisotropic structure of the Yellowstone hot spot from shear wave splitting, *J. Geophys. Res.*, *110*, B11304, doi:10.1029/2004JB003501.

Waite, G., R. B. Smith, and R. M. Allen (2006), Vp and Vs structure of the Yellowstone Hot spot upper mantle from teleseismic tomography: Evidence for an upper mantle plume, *J. Geophys. Res.*, *111*, B04303, doi:10.1029/2005JB003867.

Weeraratne, D. S., D. W. Forsyth, K. M. Fischer, and A. A. Nyblade (2003), Evidence for an upper mantle plume beneath the Tanzanian craton from Rayleigh wave tomography, *J. Geophys. Res.*, *108*(B9), 2427, doi:10.1029/2002JB002273.

West, M., W. Gao, and S. Grand (2004), A simple approach to the joint inversion of seismic body and surface waves applied to the Southwest U.S, *Geophys. Res. Lett.*, *31*, L15615, doi:10.1029/2004GL020373.

Yuan, H., and K. Dueker (2005), Teleseismic *P*-wave tomogram of the Yellowstone plume, *Geophys. Res. Lett.*, *32*, L07304, doi:10.1029/2004GL022056.

Yuan, H., K. Dueker, and D. L. Schutt (2006), Synoptic scale crustal thickness and velocity maps along the Yellowstone hot spot track, *Eos Trans. AGU*, *87*(52), Fall Meet. Suppl., Abstract S43A-1376.

Zeiler, C. P., M. C. Stickney, and M. A. Speece (2005), Revised velocity structure of Western Montana, *Bull. Seismol. Soc. Am.*, *95*(2), 759–762, doi:10.1785/0120040088.

Zhou, R.-M., and B. W. Stump (2004), Rayleigh waves generated by mining explosions and upper crustal structure around the Powder River Basin, Wyoming, *Bull. Seismol. Soc. Am.*, *94*(4), 1410–1429.

K. Dueker, D. L. Schutt, and H. Yuan, Department of Geology and Geophysics, University of Wyoming, P. O. Box 3006, Laramie, WY 82071-3006, USA. (schutt@uwyo.edu)